McGinley Lisa (Orcid ID: 0000-0003-0346-8242)

**Title:** Magnetic resonance imaging of human neural stem cells in rodent and primate brain

**Running Title**: MRI tracking of intracranial stem cell grafts

**Authors**: Lisa M. McGinley Ph.D.[1], Matthew S. Willsey M.D.[2,7], Osama N. Kashlan M.D.[1,2], Kevin S. Chen M.D.[1,2], John M. Hayes B.S.[1], Ingrid L. Bergin V.M.D. M.S.[3], Shayna N. Mason B.S.[1], Aaron W. Stebbins B.S.[1], Jacquelin F. Kwentus[1], Crystal Pacut B.S.[1], Jennifer Kollmer M.D.[4], Stacey A. Sakowski Ph.D.[1], Caleb B. Bell III Ph.D.[5,6], Cynthia A. Chestek Ph.D.[7,8,9], Geoffrey G. Murphy Ph.D.[10,11], Parag G. Patil M.D. Ph.D.[1,2,7], Eva L. Feldman M.D. Ph.D.*[1]

**Affiliations**:

[1] Department of Neurology, University of Michigan, Ann Arbor, MI, USA

[2] Department of Neurosurgery, University of Michigan, Ann Arbor, MI, USA

[3] Unit for Laboratory Animal Medicine, University of Michigan, Ann Arbor, MI, USA

[4] Department of Neuroradiology, University Hospital Heidelberg, Heidelberg, Germany

[5] Bell Biosystems, San Francisco, CA, USA

[6] G4S Capital & Ikigai Accelerator, Santa Clara, CA, USA

[7] Department of Biomedical Engineering, University of Michigan, Ann Arbor, MI, USA

[8] Department of Electrical Engineering, University of Michigan, Ann Arbor, MI, USA

[9] Neuroscience & Robotics Graduate Program, University of Michigan, Ann Arbor, MI, USA

[10] Department of Molecular & Integrative Physiology, University of Michigan, Ann Arbor, MI, USA

This is the author manuscript accepted for publication and has undergone full peer review but has not been through the copyediting, typesetting, pagination and proofreading process, which may lead to differences between this version and the Version of Record. Please cite this article as doi: 10.1002/sctm.12802

[11] Molecular & Behavioral Neuroscience Institute, University of Michigan, Ann Arbor, MI, USA

**Author Contributions**

L.M.M.: Conception and design, collection and/or assembly of data, data analysis and interpretation, manuscript writing, final approval of manuscript.

M.S.W.: Collection and/or assembly of data, data analysis and interpretation, manuscript writing, final approval of manuscript.

O.N.K.: Conception and design, collection and/or assembly of data, final approval of manuscript.

K.S.C.: Conception and design, data analysis and interpretation, manuscript writing, final approval of manuscript.

J.M.H., I.L.B., S.N.M., A.W.S., J.F.K.: C.P.: Collection and/or assembly of data, final approval of manuscript.

J.K.: Data analysis and interpretation, manuscript writing, final approval of manuscript.

S.A.S.: Manuscript writing, final approval of manuscript.

C.B.B.: Provision of study material, final approval of manuscript.

C.A.C.: Collection and/or assembly of data, data analysis and interpretation, final approval of manuscript.

G.G.M.: Conception and design, final approval of manuscript.

P.G.P.: Conception and design, collection and/or assembly of data, data analysis and interpretation, final approval of manuscript.

E.L.F.: Conception and design, financial support, final approval of manuscript.

**Correspondence Information**: Eva L. Feldman, M.D. Ph.D. Address: 5017 AAT-BSRB, 109 Zina Pitcher Place, Ann Arbor, MI 48109. Phone: 734-763-7274 / Fax: 734-763-7275 / Email: efeldman@med.umich.edu

**Acknowledgements**: This research was supported by the NIH (5U01AG057562-02, E.L.F. G.G.M. L.M.M.; R01AG052934, G.G.M.; 1R43TR001202-01, C.B.B.; T32NS007222, M.S.W. and R25NS089450, K.S.C), the A. Alfred Taubman Medical Research Institute (P.G.P.), the Handleman Emerging Scholar Program (L.M.M.), the NeuroNetwork for Emerging Therapies, the Robert E. Nederlander Sr. Program for Alzheimer's Research, and the Sinai Medical Staff Foundation. We thank Neuralstem Inc. for supplying the hNSC line used in the study and Bell Biosystems Inc. for supplying Magnelle® tracking reagents, iron assay, and Magnelle® antibody. We thank the Unit for Laboratory Animal Medicine, the *In Vivo* Animal Core, Eric Kennedy, Paras Patel, Dina Salhani and Ryan Smith at the University of Michigan for assistance with NHP care, surgical and MRI procedures and histology. We are grateful to Dr. Stephen I. Lentz and the Imaging Laboratory of the Microscopy, Imaging and Cellular Physiology Core of the Michigan Diabetes Research Center (funded by NIDDK under NIH5P60DK20572) for help with confocal imaging of whole brain sections, and the Department of Radiology at the University of Michigan for the use of the Center for Molecular Imaging and the Preclinical Imaging & Computational Analysis Shared Resource (supported in part by Comprehensive Cancer Center NIH grant P30 CA046592). We are also thankful to Prof. Sabine Heiland, PhD at the University Hospital Heidelberg for her guidance on MRI analysis.

**Keywords**:

Stem Cell Transplantation, *In vivo* tracking, Stem/progenitor cell, Cellular therapy, Cell transplantation, Nervous system.

**Word Count (excluding abstracts, tables, figures, legends, references)**: 5,128

**Pages**: 26

**References**: 49

**Tables**: 0

**Figures**: 7

**ABSTRACT**

Stem cell transplantation therapies are currently under investigation for central nervous system disorders. Although preclinical models show benefit, clinical translation is somewhat limited by the absence of reliable non-invasive methods to confirm targeting and monitor transplanted cells *in vivo*. Here, we assess a novel MRI contrast agent derived from magnetotactic bacteria, magneto-endosymbionts (MEs), as a translatable methodology for *in vivo* tracking of stem cells after intracranial transplantation. We show that ME labeling provides robust MRI contrast without impairment of cell viability or other important therapeutic features. Labeled cells were visualized immediately post-transplantation and over time by serial MRI in non-human primate and mouse brain. Postmortem tissue analysis confirmed on-target graft location, and linear correlations were observed between MRI signal, cell engraftment, and tissue ME levels, suggesting that MEs may be useful for determining graft survival or rejection. Overall, these findings indicate that MEs are an effective tool for *in vivo* tracking and monitoring of cell transplantation therapies with potential relevance to many cellular therapy applications.

## INTRODUCTION

Cell-based therapies provide a multifaceted approach for the treatment of central nervous system (CNS) disorders. Intracranial transplantation of multiple cell types is effective in animal disease models and is currently under clinical investigation for stroke, Parkinson's disease, and Alzheimer's disease [1-4]. We are currently developing a line of human neural stem cells (hNSC) as a novel therapy for Alzheimer's disease [5-8]. Our work, and that of others, shows the benefit of cell transplantation in preclinical disease models and demonstrates the safety and feasibility of targeted intracranial delivery [5, 9-12]. However, preclinical development and translation to patients is limited by ineffective methods to assess graft delivery and post-transplantation graft survival *in vivo*. Real-time information on targeting accuracy, biodistribution, and engraftment is critical to determining efficacy and developing effective targeted therapies. Assessing these parameters *in vivo* in a non-invasive manner is particularly important in the efficacious and ethical use of large animal models.

Various imaging modalities have been used to monitor cells *in vivo*, including optical and bioluminescence imaging, positron emission tomography, and magnetic resonance imaging (MRI). MRI is often the modality of choice as it avoids ionizing radiation and offers 3D imaging capacity, excellent soft tissue contrast particularly in the CNS, and high resolution. *In vivo* tracking by MRI requires either genetic modification or direct cell labeling with contrast agents. Superparamagnetic iron oxide (SPIO) nanoparticles are the most commonly used exogenous contrast agent for cell tracking and several are FDA-approved, but broad clinical use has been limited to immediate confirmation of cell transplantation [13, 14]. MR signal can significantly decrease over time as SPIO is diluted in dividing cells, and non-specific particle uptake by endogenous tissue and cells has been reported[15-24]. Furthermore, MR signal does not always correlate with graft cell viability, as *in vivo* SPIO contrast signal persists after

transplanted cell death [15, 19, 21, 25]. These limitations have made it difficult to longitudinally assess transplanted cells in long-term studies.

The recent development of novel magneto-endosymbiont (ME) contrast agents from magnetotactic bacteria may overcome many of these challenges [23, 26, 27]. MEs are derived from the non-pathogenic bacterial strain *Magnetospirillum magneticum* AMB-1, and naturally synthesize multiple chains of membrane-enclosed magnetite particles, known as magnetosomes [28, 29]. Due to their high relaxivity, MEs are robust contrast agents for T2-weighted MRI imaging [23, 26]. ME labeling of eukaryotic cells was recently shown to be an effective *in vivo* MRI tracking method, and a unique live-cell specificity feature was demonstrated in a murine myocardial infarction model [23]. However, ME-based tracking technology has not yet been examined in immunocompetent animals or large animal models after targeted intracranial transplantation.

Therefore, the purpose of this study was to evaluate ME-based cell tracking in two immunocompetent xenotransplantation models, and characterize the impact of labeling on neural cell function *in vitro* and *in vivo*. In this report, we transplanted ME-labeled hNSCs (hNSC-Mag$^{+}$) via targeted intracranial injection into the non-human primate (NHP) and mouse brain to determine the translational potential of this novel MRI contrast agent.

## MATERIALS AND METHODS

*ME labeling*

hNSCs (line HK532-CAG-IGF1) were supplied by Neuralstem, Inc. (Germantown, MD) and cultured as previously described [6, 7]. ME labeling was performed using Magnelle® reagents per manufacturer protocols (Bell Biosystems, San Francisco, CA) and published reports [23, 26, 27]. Briefly, MEs were added to cells at 60-70% confluence in antibiotic-free growth medium and incubated for approximately 16 h in normal culture conditions (5% $O_2$, 5% $CO_2$, 37°C). Cells were then washed 3 times in growth media and treated with 50 μg/mL gentamycin sulfate (Millipore, Billerica, MA) for 12-24 h to remove extracellular MEs. After antibiotic treatment, hNSC-Mag$^+$ were collected for viability assessment by standard Trypan Blue exclusion, iron quantification using a ferrozine-based Iron Assay Kit (Bell Biosystems [27]), and additional *in vitro* characterization detailed below. To visualize ME labeling, a separate population of cells were cultured on glass coverslips, labeled with MEs and after antibiotic treatment were fixed in 4% paraformaldehyde for standard immunocytochemistry using anti-Magnelle antibody (Bell Biosystems), tubulin (ab6160, Abcam, Cambridge, MA) and Hoechst nuclear stain (Sigma, St. Louis, MO; 1 mg/mL).

*In vitro characterization*

*Differentiation potential*. Cells were differentiated for 7 d on glass coverslips and standard immunocytochemistry was performed [7] using primary antibodies for differentiation markers: TUJ1 (CH23005, Neuromics, Edina, MN), MAP2 (MAB3418, Millipore), GFAP (Z0334, Dako Corporation, Carpinteria, CA), OLIG2 (Ab9610, Millipore). *Proliferation and migration*. Proliferation and migration were measured using commercially available kits as previously described [7]. For proliferation, cells on glass coverslips (on day 0 or day 7 during differentiation) were incubated with 10 μM 5′-ethynyl-2'-deoxyuridine (EdU) for 2 h before fixation and processing following manufacturer protocols for the

Click-It EdU kit (Thermo Fisher Scientific). For migration assessment, migration inserts containing cells at day 0 or day 7 of differentiation were placed into growth media plus 10 % serum. After 24 h, cells that had migrated through the insert were stained and quantified according to manufacturer protocols for the QCM 24-well Colorimetric Cell Migration Assay (Millipore). *Neurotrophic factor production.* Neurotrophic factors were measured in conditioned media from undifferentiated and differentiated cells using enzyme-linked immunosorbent assays for human-specific insulin-like growth factor 1 (IGF1; R&D Systems, Minneapolis, MN), brain-derived neurotrophic factor (BDNF; Raybiotech, Norcross, GA), and vascular endothelial growth factor (VEGF; Raybiotech). *Neuroprotection*. Neuroprotective capacity of hNSC was assessed using an established amyloid beta toxicity assay in primary embryonic cortical neurons co-cultured with or without hNSC [7].

*NHP transplantation & MRI*

All animal protocols were approved by the University of Michigan Institutional Animal Care and Use Committee, and performed according to University of Michigan guidelines and state and federal regulations. Intracranial transplantation was performed on a 14-year-old healthy female rhesus macaque (*Macaca mulatta*) weighing 9.9 kg as previously described [30]. Briefly, stereotactic surgical coordinates were obtained for the hippocampus, thalamus, and posterior cingulate using a rhesus macaque atlas [31]. Cell suspensions were prepared at 80k/μL in hibernation medium (Neuralstem, Inc.), and Trypan Blue exclusion testing ensured transplantation of >90 % viable cells. Injections were performed using an intracerebral microinjection device with a 25G needle (FHC, Inc., Bowdoin, ME), a 50 μL Syringe Barrel (Hamilton Co., Reno, NV), and a PHD 22/2000 syringe pump (10 μL/min; Harvard Apparatus, Holliston, MA). hNSC-Mag$^+$ were administered to the temporal lobe, thalamus, and posterior cingulate on the left

side (2 x 20 μL/site), and unlabeled hNSCs to the contralateral temporal lobe target (1 x 20 μL). An immunosuppressive regimen, based on previous clinical trials transplanting human stem cells [32] was adapted and administered as follows. One day prior to surgery, Tacrolimus (FK506) was administered *per os* (PO) in food (4.25 mg/kg, BID). Post-transplantation, PO medications were administered as follows: postoperative day (POD) 2, 5: 42 mg FK506, 9 mg prednisone, 140 mg mycophenolate mofetil; POD 7, 9: 40 mg FK506, 6 mg prednisone, 250 mg mycophenolate mofetil; POD 12: 40 mg FK506, 6 mg prednisone; POD 14, 16: 40 mg FK506, 6 mg prednisone, 250 mg mycophenolate mofetil; POD 19, 21: 40 mg FK506, 3 mg prednisone, 250 mg mycophenolate mofetil; POD 23: 45 mg FK506, 3 mg prednisone, 250 mg mycophenolate mofetil. The NHP was monitored daily for neurological sequelae (e.g. level of arousal, paresis, incoordination) and wound healing. Plasma FK506 was assessed by peripheral blood draw at various postoperative time points. MR images were obtained on a GE SIGNA MR750 3.0 Tesla system with an 8-channel HR Brain Array head coil (GE Healthcare, Waukesha, WI), 1 month preoperatively, and at POD 7, 14, and 28. The NHP was anesthetized with 4-6 mg/kg Tiletamine/Zolazepam (Telazol®) and maintained with 2-4 % isoflurane for the duration of imaging procedures. Images were acquired using T2*-weighted spoiled gradient echo sequences with the following parameters: repetition time (TR)/effective echo time (TE), 30/11.3 ms; flip angle 5; field of view (FOV) 19.2 $mm^2$, matrix size 512 x 512; slice thickness 2mm; receiver bandwidth 195 Hz/Px; acquisition time approximately 70 min.

*Mouse transplantation & MRI*

Intracranial transplantation was performed on 16-week-old male C57BL/6J mice (Jackson Laboratory, Bar Harbor, ME) using our established stereotactic approach [5-7]. Briefly, mice were

anesthetized with 2% isoflurane and placed in a standard Kopf stereotactic frame (David Kopf Instruments, Tujunga, CA). hNSC suspensions were prepared at 30k/µL in hibernation medium (Neuralstem, Inc.), and Trypan Blue exclusion ensured transplantation of >90% viable cells. hNSCs were delivered by bilateral injection to the fimbria of the hippocampus at 3 sites (3 x 1 µL hNSC-Mag$^+$ left hemisphere and 3 x 1 µL unlabeled hNSCs contralateral; each administered over 60 s) at the following coordinates (bregma/lateral/ventral): -0.82/0.75/2.5, -1.46/2.3/2.9, -1.94/2.8/2.9 mm, totaling 90k hNSCs per hemisphere per animal. All animals received immunosuppression of subcutaneous mycophenolate mofetil (30 mg/kg daily) until POD 7 and FK506 (3 mg/kg daily) for the study duration. MRI was performed on a GE-Agilent 9.4 Tesla horizontal bore system (GE Healthcare) at POD 7, 28, 42, and 70. Mice were anesthetized with 2% isoflurane and body temperature maintained at 37°C for the duration of imaging procedures. A quadrature volume radiofrequency coil was used to scan the head region of the mice. Axial T2*-weighted images were acquired using a gradient echo sequence with the following parameters: TR/TE 300/6 ms; flip angle 20; FOV 20x20 mm$^2$; matrix size 256x128; slice thickness 0.5 mm; number of slices 25; acquisition time 2.5 min. All MR images were viewed and graft signal volumes calculated using ImageJ. Briefly, the ME contrast agent induces a susceptibility artifact on T2* weighted images, so that hypointense signal can be regarded as the MRI correlate of hNSC-Mag$^+$. Hypointense signal was measured in regions of interest containing labeled cell grafts and unlabeled control cell grafts. Any hypointense signal detected on the control side was used as a threshold to be exceeded on the contralateral side in order to be counted as signal derived from labeled cells. For each animal, the graft area was measured on each slice where the graft was visible (approximately 5-10 slices per animal), summed for all slices and subsequently multiplied by the slice thickness (0.5 mm). The presented data represent total graft area signal volume per animal per time point (mm$^3$).

*Tissue histology*

The NHP was euthanized on POD 29, and the brain was harvested and processed for histology and immunohistochemistry as previously described [30]. Briefly, the brain tissue was trimmed, cassetted, and fixed in 3.7% paraformaldehyde. Following standard paraffin processing, 4 µm sections were stained with hematoxylin and eosin for injection site visualization or Perls' Prussian Blue for iron detection. Immunostaining was performed using primary antibodies for STEM121 (Y40410, Takara, Mountain View, CA), CD3 (RM9107, clone SP7, Fisher Scientific), CD68 (ab955, clone KP1, Abcam), GFAP (ab7260, Abcam) and Magnelles (Bell Biosystems). Subsets of mice were euthanized on POD 7, 28, and 70 (n=3 per time point) directly after completion of MRI. Plasma FK506 was measured in peripheral blood obtained from the inferior vena cava. Mice were perfused with saline and 4% paraformaldehyde, and whole brains were post-fixed in 4% paraformaldehyde, cryoprotected in 30% sucrose, and cryosectioned (coronal, 40 µm). Immunostaining was performed using primary antibodies for human nuclei (huNu; MAB1281, Millipore), Magnelles (Bell Biosystems), NeuN (ab104225, Abcam), GFAP (Z0334, Dako), hNestin (ABD69, Millipore), and Hoechst nuclear stain (Sigma; 5 mg/mL). Grafted hNSC were quantified in images captured from fimbria fornix target areas using the ImageJ multi-point tool (6 images/section; 10 sections/mouse). ME-derived iron was measured in the same regions using ImageJ, providing a composite measure of fluorescent intensity and area.

*Statistics*

Statistical significance was determined using Prism 8 (GraphPad Software Inc., La Jolla, CA) and an alpha-level of 0.05. Brown-Forsythe F-tests were used to compare variances and determine distribution. Data were analyzed by parametric t-test, one-way analysis of variance (ANOVA) with Tukey's post-test for comparisons of multiple groups, or Pearson's correlation. *In vitro* data are presented as mean ± SEM or as representative images of at least three independent labeling experiments (n=3-6 per condition). Sample size for *in vivo* experiments: NHP (n=1) and mouse (n=3 per POD time point).

## RESULTS

*ME labeling, iron loading, and cell viability*

To assess ME incorporation and post-labeling viability, hNSCs were initially labeled with ME labeling ratios (MLR) of 2k, 4k, and 6k particles per cell. No differences in hNSC-Mag$^+$ morphology were observed by bright field imaging and all groups appeared morphologically healthy (Fig.1A). ME incorporation was visualized using a Magnelle-specific antibody and tubulin to label cell borders. ME particles appeared punctate and localized to the perinuclear area of the cell (Fig.1B). No particles were found in unlabeled cell groups. Assessment of labeling efficiency revealed an average intracellular iron content that significantly increased with higher MLRs and ranged from 0.45 ± 0.12 pg/cell at 2k MLR, to 0.82 ± 0.09 pg/cell at 6k MLR (Fig.1C). At the tested MLRs, there were no significant differences in viability compared to controls, with >97% viability across all groups (Fig.1D).

*ME labeling does not impact hNSC functional properties in vitro*

To assess biocompatibility, the basic cell functions of labeled hNSC-Mag$^+$ with an iron content of 0.4-0.5 pg/cell were compared to unlabeled hNSC. Differentiation potential was maintained post-labeling, with similar expression patterns between labeled and unlabeled cells for markers of immature neurons (TUJ1$^+$), mature neurons (MAP2$^+$), astrocytes (GFAP$^+$), and oligodendrocytes (OLIG2$^+$) (Fig.2A). Migratory and proliferative capacity throughout differentiation was also maintained (Fig.2B-C). An important therapeutic feature of this hNSC line is the production of various secreted neurotrophic factors, including BDNF, IGF1, and VEGF. Here, quantified levels of secreted BDNF, IGF1, and VEGF were maintained throughout differentiation, with no significant changes measured post-labeling (Fig.2D-F). The impact of MEs on neuroprotective function was determined using an established toxicity assay in cortical neurons co-cultured with or without hNSC. Apoptosis was significantly reduced when co-cultured with hNSC or hNSC-Mag$^+$ (cortical neurons alone, 64.9 ± 2.7%; hNSC, 14.6 ± 7.5%; hNSC-Mag$^+$, 14.96 ± 3.1%; ANOVA; $p<0.05$), indicating that neuroprotective capacity was unaffected by MEs (Fig.2G). Finally, the stability of ME labeling was determined in frozen stocks of hNSC-Mag$^+$ and in hNSC-Mag$^+$ cultured for 7 d, where intracellular iron was not significantly different from freshly labeled cells (data not shown). Collectively, these data demonstrate that ME particles are biocompatible with hNSCs, and that ME labeling resulting in an intracellular iron content of 0.4-0.5 pg/cell does not impact important therapeutic features of this cell line.

*ME-enabled MRI tracking of hNSC in vivo*

To assess the feasibility of ME-based tracking in a large animal model, intracranial transplantation was performed in a single NHP. hNSC-Mag$^+$ were delivered to temporal, thalamus, and cingulate targets, and a single contralateral temporal targeted injection of unlabeled hNSC was performed as a control. T2*-

weighted MRI was performed at various time points for 28 d after transplantation to identify ME-labeled transplanted cells (Fig.3). At POD 7, hNSC-Mag$^+$ grafts were identified as hypointense MR signal at all three hNSC-Mag$^+$ transplantation sites compared to the contralateral control injection site of unlabeled cells. By POD 14, the intensity of the left temporal and cingulate targets had decreased to that of the contralateral control site. The highest hypointense MR signal was observed at the thalamic target initially at POD 7, and, although there was a gradual decline over time, by POD 28 hypointense MR signal at this site was still increased compared to the control site and the hNSC-Mag$^+$ temporal and cingulate sites.

We next further validated MRI tracking in mice, which enabled parallel evaluation of MR and tissue signal at multiple post-transplant time points. Intracranial transplantation was performed in C57BL/6J mice, with injection of 90k hNSC-Mag$^+$ and a contralateral internal control of 90k unlabeled hNSC (Fig.4A), and serial T2*-weighted MRI tracking was used to follow cell grafts for up to 10 weeks post-transplantation (Fig.4B). At POD 7, hNSC-Mag$^+$ grafts were detected as hypointense signal localized to the fimbria fornix target site in the hNSC-Mag$^+$ hemisphere in all transplanted mice (n=9 total). Negligible hypointense signal was observed at earlier time points on the contralateral side injected with control unlabeled cells, likely due to small areas of hemorrhage within injection tracts and tissue disruption at the surgical site. Quantification of MR signal for all mice and all time points (Fig.4C) revealed a variable signal volume at POD 7 that averaged $1.12 \pm 0.2$ mm$^3$. By POD 28, the average signal volume was $0.88 \pm 0.2$ mm$^3$, but this decrease was not significant ($p = 0.462$). In the subset of mice followed by serial MRI for 10 weeks (n=3), initial average volumes were $1.35 \pm 0.31$ mm$^3$ at POD 7, and gradually declined over the next 8 weeks ($0.98 \pm 0.14$ mm$^3$ at POD 56). By POD 70, signal volume was significantly reduced to $0.47 \pm 0.09$ mm$^3$ ($p<0.05$ vs. POD 7, 28, 56).

*Postmortem histological validation of MR signal*

Histological analysis of NHP brain tissue was performed one day after the final MRI on POD 29 (Fig.5). To explore whether the thalamic T2* hypointensity correlated with engrafted hNSCs, this site was analyzed in detail. Intact hNSCs were not detected morphologically or by immunostaining for human-specific STEM121 (Fig.5C-D). Injection sites were consistent with localized neuropil damage and phagocytosis of debris by activated macrophages. Infiltrating cells were composed primarily of macrophages ($CD68^+$), with fewer T cells ($CD3^+$), and a border of astrocytes ($GFAP^+$) (Fig.5E-G). These areas were positive for iron and ME particles (Fig.5H-I). ME- and iron-containing debris within the extracellular space corresponded to the area of tissue damage and intracellular cytoplasmic staining corresponded to macrophages ($CD68^+$ in serial sections), suggesting graft rejection and clearance by resident phagocytic macrophages. Postoperative monitoring of immunosuppressant FK506 levels in the NHP until endpoint indicated that target plasma levels within the range of 20-40 ng/mL were reached on POD 7; however, after this time point, levels dropped to < 1 ng/mL due to variable success of oral PO dosing.

In mice, transplanted cell grafts were evaluated histologically at multiple time points, directly following MRI at POD 7, 28, and 70 (Fig.6). MR signal corresponded with huNu and ME immunostaining signal, most evident at the earlier time point where large grafts were visible, while contralateral control grafts exhibited huNu staining but no ME signal (Fig.6A,B). At high magnification, MEs colocalized with intact human cells ($huNu^+$) and no ME staining was present on the contralateral control side (Fig.6C). Similar to *in vitro* immunostaining, ME particles appeared punctate and localized to the perinuclear area of the cell, indicating that ME labeling persists after *in vivo* transplantation. However, by the later terminal time points, the grafts had reduced in size, demonstrated by diminished huNu and

ME signal (Fig.6D-I). ME and huNu$^+$ debris was observed in the target areas, indicative of graft rejection. Quantification showed a significant decline in huNu$^+$ nuclei and ME signal over time, in line with MRI data (Fig.6J-L). A reduction of up to 80% occurred at POD 28 and POD 70, compared to the early time point ($p<0.05$ vs. POD 7). Linear correlations were observed between ME and MR signal ($r=0.6964$, $p=0.0372$), cell engraftment and MR signal ($r=0.7059$, $p=0.0336$), and ME and cell engraftment ($r=0.7756$, $p=0.0140$) (Fig.6M-O). Measurement of immunosuppressant FK506 levels at endpoint were below target range in the later cohorts despite evidence of target plasma levels of 20-40 ng/mL in POD 7 mice.

Mouse brain tissue was further analyzed across the terminal post-transplant time points to determine if ME labeling influences hNSC phenotype *in vivo*. No changes in cell distribution were observed between unlabeled hNSC and hNSC-Mag$^+$ grafts (Fig.6B,D,F). Importantly, characterization of cell fate also indicated that ME labeling did not impact differentiation, as there were no changes in marker expression between hNSC-Mag$^+$ and contralateral control hNSC grafts (Fig.7). At POD 7, hNSC and hNSC-Mag$^+$ grafts expressed differentiation markers of early neural progenitor cells (human nestin$^+$), but did not express markers of astrocytes or mature neurons (GFAP or NeuN). At the later POD 28 and 70 time points, no changes were observed between hNSC-Mag$^+$ and contralateral control hNSC graft sites; however, grafts were significantly reduced, with few intact huNu$^+$ cells visible within the injection tracts.

## DISCUSSION

Reliable and precise detection and tracking of transplanted cells is essential for understanding and advancing the field of stem cell therapies. In this study, we evaluated ME-based cell tracking in two

immunocompetent xenotransplantation models and characterized the impact of labeling on neural cell function *in vitro* and *in vivo*. Our results show that hNSCs can be efficiently labeled with ME particles without affecting cell viability or other important *in vitro* functional properties. We also demonstrate, for the first time, MRI visualization and tracking of ME-labeled hNSCs in immunocompetent NHP and murine brain. In NHP brain, ME labeling enabled the detection of transplanted cells and their precise location by MRI, although engrafted hNSCs were not detected postmortem, consistent with diminished MR signal. In mice, MR signal was indicative of graft location and also correlated with postmortem tissue ME levels and engrafted hNSC nuclei. Unlike other iron-based labeling methods, the correlation between MR signal and cell engraftment suggests that with further optimization ME-based particles may be a useful method for determining graft rejection *in vivo*. Overall, these findings indicate that MEs are an effective tool for *in vivo* monitoring of cell-based therapies and may be easily applied to other cell lines and CNS diseases. Our use of a human cell product and two immunocompetent animal models, including a large animal model, make this report particularly relevant to translational pipelines and investigational new drug-enabling applications.

Our extensive *in vitro* characterization of ME-labeled hNSCs supports the contention that MEs are biocompatible. We showed that MEs are non-toxic to hNSCs, with no overt changes in survival, growth, or morphology. Importantly, ME labeling also did not alter therapeutically relevant cell functions, including production of secreted neurotrophic factors and neuroprotective capacity. MEs have previously been used to label 231BR, a human breast adenocarcinoma line, and human induced pluripotent stem cell (iPSC)-derived cardiomyocytes [23, 26]; however, labeling efficiency is cell-type dependent and parameters require optimization on an individual basis. In this first report using MEs to label a neural cell type, we showed that hNSCs could be loaded with MEs with no detectable toxicity at any labeling ratio.

Ideally, any modification or labeling for MRI contrast must not compromise the biological functioning of specific cell types. This safety aspect is critical to the translation of tracking technologies to clinical studies. Several reports indicate that SPIO labeling can negatively impact cell function. A deleterious dose-dependent effect on chondrogenesis was shown in mesenchymal stem cells [33, 34] and changes in neuronal and glial differentiation and migration were reported in neural precursors [19, 35, 36]. Conversely, others have found no negative effect of SPIO or other magnetic nanoparticles on growth, morphology, viability, or proliferation of neural progenitor cells, iPSC, and embryonic stem cells [14, 20, 37-39]. Although not as well characterized as SPIO-based agents, ME labeling was previously shown to not impact the short-term cardiac properties of cardiomyocytes [23], suggesting that MEs are biocompatible. However, the impact of MEs on neural cell biology and functional properties had not yet been determined. We therefore assessed multiple aspects of cell function in a series of established assays [7, 40]. Contrary to findings that SPIO-based reagents disrupt normal differentiation patterns, we found that *in vitro* hNSC differentiation was unchanged by ME labeling. Similarly, proliferation, migration, production of neurotrophic growth factors BDNF, IGF1, and VEGF, and neuroprotective capacity were unchanged in undifferentiated and differentiated cell states. Collectively, these data demonstrate that MEs are biocompatible with this line of hNSCs and do not negatively impact important therapeutic features. Furthermore, we demonstrated the longevity and stability of ME labeling, where intracellular iron levels were retained after additional culturing and in frozen stocks, validating the use of hNSC-Mag$^+$ for *in vivo* transplantation purposes.

Our transplantation studies in two animal models verify that ME labeling enables visualization and tracking of hNSCs *in vivo* by MRI. To our knowledge, this is the first report to demonstrate MRI tracking of transplanted human stem cells in the NHP brain. Transplanted hNSC-Mag$^+$ were clearly identified in

temporal, thalamus, and cingulate targets of the NHP brain by serial 3T MRI scans one week after transplantation, and up to 4 weeks postoperatively. Difficulty in administering PO immunosuppressant to this NHP resulted in insufficient plasma levels of FK506 after the first MRI scan. This, however, permitted correlation between MR signal and hNSC-Mag$^+$ viability in a host with restored immune competency. Consequently, MR signal decreased over time, which was reflected in postmortem histological analysis showing minimal engraftment at 4 weeks post-transplant. At this point, no intact hNSCs were detected either morphologically or using human specific markers, despite extensive sectioning in the target areas. Immunohistochemistry profiling of the injection sites showed infiltrating immune cells and intracellular and extracellular staining for ME and iron particulates or remnants, suggesting that hNSC-Mag$^+$ grafts were undergoing tissue clearance by phagocytic cells and perivascular flow. The observed decline in MR signal over time was therefore caused by transplanted cell death and clearance of ME particles. It is well established that immunosuppression is required to prevent rejection of allografts or xenografts in NHP [41-43], and these data are in line with multiple reports of poor engraftment and high rates of rejection of human cells after transplantation in other large animal models [19, 44, 45].

We further assessed ME tracking in a longitudinal study in rodents, which enabled postmortem tissue analysis and quantification in multiple animals at several post-transplant time points. This parallel study in mice validated our key findings in the NHP. On-target hNSCs were clearly identified in the fimbria fornix of all mice by 7T MRI. MR signal diminished over time and corresponded with histological hNSC-Mag$^+$ grafts and ME particles. Engraftment was most robust at one-week post-transplant, and ME particles were visible localized to intact hNSCs. Engraftment was reduced at the two later time points, consistent with the diminished MR signal. The linear correlations observed between MR signal, ME

tissue signal, and cell engraftment suggest that with further optimization this approach may be useful for determining long-term graft survival or rejection *in vivo*. Subtherapeutic FK506 levels are again a likely reason for graft rejection at later time points, and observed post-transplant cell survival is consistent with our ongoing studies and published reports in rodents [11, 42, 46].

In the literature, there is extensive evidence that residual extracellular or intramacrophagic iron from SPIO-based detection labels results in false MR signal long after transplanted cell death [15-24]. This overestimation of cell survival limits the interpretation of long-term MRI tracking using such detection methods. SPIO particles have been detected extracellularly and within macrophages for months after transplanted cell death in myocardial infarction models [21, 23, 24]. In rodent brain, particles persisted from 1-5 months with no correlating engraftment [14, 15, 20]. Similarly, in minipig spinal cord, rejected cell grafts retained histologic iron, and MR signal also did not correlate with engraftment [19]. Initial studies indicate that MEs clear from tissue more rapidly - reportedly within one week of cell death in the myocardium based on MR signal [23]. This concept of live cell specificity unique to MEs has been associated with immune system interactions and is supported by previous studies using purified magnetosomes isolated from magnetotactic bacteria strains [47-49]. In rats, magnetosomes were rapidly removed from the circulation via lysosomal digestion and clearance mediated by the reticuloendothelial system, also known as the mononuclear phagocyte system, comprised primarily of macrophages. ME antigenicity, relative to the inert coating of SPIO particles, combined with the release of proteins, nucleic acids, and polysaccharides after cell death, likely contribute to the targeting and clearance of magnetotactic bacteria and their associated magnetic particles by the immune system. However, the persistence of histological detection after cell death in the brain is unknown. Clearance likely depends on target tissue, vascularization, and activity of phagocytosing immune cells. Here, we observed a

persistence of MR signal after transplanted cell death; however, unlike previous SPIO studies, there was a significant reduction in MR signal over time, which was detectable visually in NHP and by quantification of hypointense volume in mice. Moreover, in mice, histologic ME particles correlated with MR signal and engraftment, and by the later time points, ME particles were significantly reduced in rejected cell grafts. Thus, the overestimation of cell survival due to persistence of labeling particles may not be as much of a problem with ME tracking as with SPIO-based methods.

This study has limitations. Our data showing ME biocompatibility and proof of concept ME-based *in vivo* tracking are limited to a single human neural stem cell line that is currently under therapeutic development for Alzheimer's disease as part of the NIA Alzheimer's Drug Development Program (5U01AG057562). The feasibility of MEs as effective contrast agents must also be established for other cell types of interest, such as those derived from iPS or ES cells. Our data provide evidence of *in vitro* biocompatibility and establishes feasibility *in vivo*, but it was not possible to assess these parameters *in vivo* in the long term due to eventual graft rejection in immunocompetent models. Although this provided an important opportunity to correlate MR signal and transplanted cell viability over time as host immune competency was restored, additional studies are needed with adequate immunosuppression protocols in place so that long-term tracking and biocompatibility can be investigated. Many cellular therapy approaches based on non-autologous cells will require immunosuppression and while this presents significant challenges, it represents the most clinically relevant scenario. Identification and optimization of such protocols are vital to ensure the translational relevance of preclinical transplantation studies. The study also has strengths. Our data suggest that MEs are advantageous over other contrast agents in that they are rapidly cleared from rejected grafts as the host immune response is mounted. Additional reports of *in vivo* clearance of purified magnetosomes described above also support this assertion. However,

further study is required with additional MLRs in combination with a complementary reporter gene system, such as bioluminescence, and direct comparison to SPIO, to fully validate MEs as an accurate indicator of cell survival after intracranial transplantation.

## SUMMARY

To summarize, we report MEs as a useful preclinical tool for non-invasive MRI tracking of transplanted cells. Our results demonstrate their value as an *in vivo* indicator of graft location, volume, targeting accuracy, and engraftment. These data and currently available literature indicate that MEs are safe and fulfill many of the requirements of an ideal MRI contrast agent for cell tracking. However, additional long-term studies are needed to further develop the unique live-cell specificity feature for CNS applications. As cell-based therapies continue to progress through translational pipelines, the development of reliable technology to identify and monitor transplanted cells *in vivo* becomes increasingly important. A multi-modal imaging strategy will most likely be utilized in future clinical settings to resolve current limitations of individual tracking techniques. The timely development of novel approaches such as this will undoubtedly advance the field of *in vivo* stem cell tracking and move us closer to developing effective treatments for patients with Alzheimer's disease and other CNS disorders.

## DISCLOSURE OF POTENTIAL CONFLICTS OF INTEREST

E.L.F. is an unpaid consultant to Neuralstem, Inc., which owns patent rights to the hNSC line used in this study, is on an advisory board for Novartis, declared research funding from the National Institutes of Health (U01 AG057562-02). P.G.P declared consultant/Advisory role with NeuroOne, Medtronic and stock interest in NeuroOne. C.B.B. was employed by Bell Biosystems Inc., which supplied the patented Magnelle reagents, but was not involved in data acquisition or analysis. This company is no longer operational. J.K. declared advisory role Akcea Therapeutics, speaker honoraria, research and travel grant from Alnylam Pharmaceuticals. All other authors disclosure no potential conflicts of interest.

## DATA AVAILABILITY STATEMENT

The data that support the findings of this study are available from the corresponding author upon reasonable request

## REFERENCES


1. Garitaonandia, I., et al., *Neural Stem Cell Tumorigenicity and Biodistribution Assessment for Phase I Clinical Trial in Parkinson's Disease.* Sci Rep, 2016. **6**: p. 34478.
2. Kalladka, D., et al., *Human neural stem cells in patients with chronic ischaemic stroke (PISCES): a phase 1, first-in-man study.* Lancet, 2016. **388**(10046): p. 787-96.
3. Kim, H.J., et al., *Stereotactic brain injection of human umbilical cord blood mesenchymal stem cells in patients with Alzheimer's disease dementia: A phase 1 clinical trial.* Alzheimers Dement (Amst), 2015. **1**(2): p. 95-102.
4. Steinberg, G.K., et al., *Clinical Outcomes of Transplanted Modified Bone Marrow-Derived Mesenchymal Stem Cells in Stroke: A Phase 1/2a Study.* Stroke, 2016. **47**(7): p. 1817-24.
5. McGinley, L.M., et al., *Human neural stem cell transplantation improves cognition in a murine model of Alzheimer's disease.* Sci Rep, 2018. **8**(1): p. 14776.
6. McGinley, L.M., et al., *Human neural stem cell transplantation into the corpus callosum of Alzheimer's mice.* Ann Clin Transl Neurol, 2017. **4**(10): p. 749-755.
7. McGinley, L.M., et al., *Human Cortical Neural Stem Cells Expressing Insulin-Like Growth Factor-I: A Novel Cellular Therapy for Alzheimer's Disease.* Stem Cells Transl Med, 2016.
8. Schweitzer, J.S., et al., *Personalized iPSC-Derived Dopamine Progenitor Cells for Parkinson's Disease.* N Engl J Med, 2020. **382**(20): p. 1926-1932.
9. Ager, R.R., et al., *Human neural stem cells improve cognition and promote synaptic growth in two complementary transgenic models of Alzheimer's disease and neuronal loss.* Hippocampus, 2014.
10. Bali, P., et al., *Neurotrophic Factors Mediated Activation of Astrocytes Ameliorate Memory Loss by Amyloid Clearance after Transplantation of Lineage Negative Stem Cells.* Mol Neurobiol, 2019.
11. Duncan, T. and M. Valenzuela, *Alzheimer's disease, dementia, and stem cell therapy.* Stem Cell Res Ther, 2017. **8**(1): p. 111.
12. Lee, I.S., et al., *Human neural stem cells alleviate Alzheimer-like pathology in a mouse model.* Mol Neurodegener, 2015. **10**(1): p. 38.
13. Bulte, J.W., et al., *Neurotransplantation of magnetically labeled oligodendrocyte progenitors: magnetic resonance tracking of cell migration and myelination.* Proc Natl Acad Sci U S A, 1999. **96**(26): p. 15256-61.
14. Guzman, R., et al., *Long-term monitoring of transplanted human neural stem cells in developmental and pathological contexts with MRI.* Proc Natl Acad Sci U S A, 2007. **104**(24): p. 10211-6.
15. Berman, S.C., et al., *Long-term MR cell tracking of neural stem cells grafted in immunocompetent versus immunodeficient mice reveals distinct differences in contrast between live and dead cells.* Magn Reson Med, 2011. **65**(2): p. 564-74.

16. Bernsen, M.R., et al., *Nanoparticles and clinically applicable cell tracking.* Br J Radiol, 2015. **88**(1054): p. 20150375.
17. Cromer Berman, S.M., P. Walczak, and J.W. Bulte, *Tracking stem cells using magnetic nanoparticles.* Wiley Interdiscip Rev Nanomed Nanobiotechnol, 2011. **3**(4): p. 343-55.
18. Cupaioli, F.A., et al., *Engineered nanoparticles. How brain friendly is this new guest?* Prog Neurobiol, 2014. **119-120**: p. 20-38.
19. Lamanna, J.J., et al., *Ferumoxytol Labeling of Human Neural Progenitor Cells for Diagnostic Cellular Tracking in the Porcine Spinal Cord with Magnetic Resonance Imaging.* Stem Cells Transl Med, 2017. **6**(1): p. 139-150.
20. Ramos-Gomez, M., E.G. Seiz, and A. Martinez-Serrano, *Optimization of the magnetic labeling of human neural stem cells and MRI visualization in the hemiparkinsonian rat brain.* J Nanobiotechnology, 2015. **13**: p. 20.
21. Chen, I.Y., et al., *Comparison of optical bioluminescence reporter gene and superparamagnetic iron oxide MR contrast agent as cell markers for noninvasive imaging of cardiac cell transplantation.* Mol Imaging Biol, 2009. **11**(3): p. 178-87.
22. Kim, J.A., et al., *Role of cell cycle on the cellular uptake and dilution of nanoparticles in a cell population.* Nat Nanotechnol, 2011. **7**(1): p. 62-8.
23. Mahmoudi, M., et al., *Novel MRI Contrast Agent from Magnetotactic Bacteria Enables In Vivo Tracking of iPSC-derived Cardiomyocytes.* Sci Rep, 2016. **6**: p. 26960.
24. Terrovitis, J., et al., *Magnetic resonance imaging overestimates ferumoxide-labeled stem cell survival after transplantation in the heart.* Circulation, 2008. **117**(12): p. 1555-62.
25. Bernau, K., et al., *In Vivo Tracking of Human Neural Progenitor Cells in the Rat Brain Using Magnetic Resonance Imaging Is Not Enhanced by Ferritin Expression.* Cell Transplant, 2016. **25**(3): p. 575-92.
26. Brewer, K.D., et al., *Characterization of Magneto-Endosymbionts as MRI Cell Labeling and Tracking Agents.* Mol Imaging Biol, 2018. **20**(1): p. 65-73.
27. Lee, K.R., et al., *Cell Labeling with Magneto-Endosymbionts and the Dissection of the Subcellular Location, Fate, and Host Cell Interactions.* Mol Imaging Biol, 2018. **20**(1): p. 55-64.
28. Komeili, A., *Molecular mechanisms of compartmentalization and biomineralization in magnetotactic bacteria.* FEMS Microbiol Rev, 2012. **36**(1): p. 232-55.
29. Benoit, M.R., et al., *Visualizing implanted tumors in mice with magnetic resonance imaging using magnetotactic bacteria.* Clin Cancer Res, 2009. **15**(16): p. 5170-7.
30. Bentley, J.N., et al., *A simple, inexpensive method for subcortical stereotactic targeting in nonhuman primates.* J Neurosci Methods, 2018. **305**: p. 89-97.
31. Saleem, K. and N. Logothetis, *A Combined MRI and Histology Atlas of the Rhesus Monkey Brain in Stereotaxic Coordinates*. 2nd Edition ed. 2012: Academic Press.
32. Glass, J.D., et al., *Transplantation of spinal cord-derived neural stem cells for ALS: Analysis of phase 1 and 2 trials.* Neurology, 2016. **87**(4): p. 392-400.
33. Kostura, L., et al., *Feridex labeling of mesenchymal stem cells inhibits chondrogenesis but not adipogenesis or osteogenesis.* NMR Biomed, 2004. **17**(7): p. 513-7.
34. Roeder, E., et al., *Dose-response of superparamagnetic iron oxide labeling on mesenchymal stem cells chondrogenic differentiation: a multi-scale in vitro study.* PLoS One, 2014. **9**(5): p. e98451.
35. Eamegdool, S.S., et al., *Ultrasmall superparamagnetic iron oxide nanoparticle prelabelling of human neural precursor cells.* Biomaterials, 2014. **35**(21): p. 5549-64.

36. Kallur, T., et al., *Spatio-temporal dynamics, differentiation and viability of human neural stem cells after implantation into neonatal rat brain.* Eur J Neurosci, 2011. **34**(3): p. 382-93.
37. Parsa, H., et al., *Effect of Superparamagnetic Iron Oxide Nanoparticles-Labeling on Mouse Embryonic Stem Cells.* Cell J, 2015. **17**(2): p. 221-30.
38. Ruan, J., et al., *Efficient preparation and labeling of human induced pluripotent stem cells by nanotechnology.* Int J Nanomedicine, 2011. **6**: p. 425-35.
39. Shen, W.B., et al., *Human neural progenitor cells retain viability, phenotype, proliferation, and lineage differentiation when labeled with a novel iron oxide nanoparticle, Molday ION Rhodamine B.* Int J Nanomedicine, 2013. **8**: p. 4593-600.
40. Lunn, J.S., et al., *Autocrine Production of IGF-I Increases Stem Cell-Mediated Neuroprotection.* Stem Cells, 2014.
41. Aron Badin, R., et al., *MHC matching fails to prevent long-term rejection of iPSC-derived neurons in non-human primates.* Nat Commun, 2019. **10**(1): p. 4357.
42. Diehl, R., et al., *Immunosuppression for in vivo research: state-of-the-art protocols and experimental approaches.* Cell Mol Immunol, 2017. **14**(2): p. 146-179.
43. Morizane, A., et al., *Direct comparison of autologous and allogeneic transplantation of iPSC-derived neural cells in the brain of a non-human primate.* Stem Cell Reports, 2013. **1**(4): p. 283-92.
44. Gutierrez, J., et al., *Preclinical Validation of Multilevel Intraparenchymal Stem Cell Therapy in the Porcine Spinal Cord.* Neurosurgery, 2015. **77**(4): p. 604-12; discussion 612.
45. Pluchino, S., et al., *Human neural stem cells ameliorate autoimmune encephalomyelitis in non-human primates.* Ann Neurol, 2009. **66**(3): p. 343-54.
46. Anderson, A.J., et al., *Achieving stable human stem cell engraftment and survival in the CNS: is the future of regenerative medicine immunodeficient?* Regen Med, 2011. **6**(3): p. 367-406.
47. Liu, R.T., et al., *Heating effect and biocompatibility of bacterial magnetosomes as potential materials used in magnetic fluid hyperthermia.* Progress in Natural Science-Materials International, 2012. **22**(1): p. 31-39.
48. Sun, J., et al., *Biocompatibility of bacterial magnetosomes: acute toxicity, immunotoxicity and cytotoxicity.* Nanotoxicology, 2010. **4**(3): p. 271-83.
49. Sun, J.B., et al., *Targeted distribution of bacterial magnetosomes isolated from Magnetospirillum gryphiswaldense MSR-1 in healthy Sprague-Dawley rats.* J Nanosci Nanotechnol, 2009. **9**(3): p. 1881-5.

## FIGURE LEGENDS

**Figure 1. ME labeling of hNSC**. Brightfield imaging of unlabeled control hNSC and ME-labeled hNSC (hNSC-Mag$^+$), with increasing MLR **(A)**. Scale bar 100 µm. Representative immunostaining showing ME localization (red) and tubulin cytoskeleton (green) in hNSC-Mag$^+$ and control unlabeled hNSC **(B)**. Scale bar 50 µm. Increased iron levels (Fe) with increasing MLR, *$p<0.05$ (ANOVA) **(C)**. Viability measured by Trypan Blue dye exclusion **(D)**. Data are presented as mean ± SEM or are representative images of at least three independent labeling experiments (n=3-6 per condition). Abbreviations: hNSC, human neural stem cells; ME, magneto-endosymbiont; MLR, ME loading ratio.

**Figure 2. *In vitro* cellular function is unchanged by ME labeling**. Representative immunostaining of hNSC and ME-labeled hNSC (hNSC-Mag$^+$) stained with TUJ1, MAP2, GFAP and OLIG2 after 7 days of differentiation **(A)**. Scale bar 50 µm. Migration **(B)**, proliferation **(C)**, and production of neurotrophic factors BDNF, IGF1 and VEGF **(D-F)** in undifferentiated (D0) and differentiated (D7) hNSC and hNSC-Mag$^+$. β-amyloid toxicity in embryonic cortical neurons alone, or co-cultured with hNSC or hNSC-Mag$^+$ as a measure of neuroprotective capacity, **$p<0.005$, embryonic cortical neurons vs. all groups (ANOVA) **(G)**. Data are presented as mean ± SEM or are representative images of at least three independent labeling experiments (n=3-6 per condition). Abbreviations: hNSC, human neural stem cells; ME, magneto-endosymbiont; TUJ1, beta III tubulin; MAP2, Microtubule Associated Protein 2; GFAP, glial fibrillary acidic protein; OLIG2, Oligodendrocyte Transcription Factor 2; BDNF, brain-derived neurotrophic factor; IGF1, insulin-like growth factor 1; VEGF, vascular endothelial growth factor; eCN, embryonic cortical neurons.

**Figure 3. *In vivo* tracking of hNSC-Mag$^+$ grafts in the NHP brain.** Representative NHP serial T2* MRI sequence scans performed on POD 7, 14, and 28. hNSC-Mag$^+$ grafts are visible as hypointense signal or dark contrast at the targeted temporal, thalamus, and cingulate sites (red circles). Control unlabeled hNSC grafts were not well visualized after transplantation to a single temporal target site (green circles). Scale bars 1 cm. Data are presented as representative MRI scans from a single NHP (n=1). Abbreviations: NHP, non-human primate; MRI, magnetic resonance imaging; POD, postoperative day; hNSC, human neural stem cells.

**Figure 4. *In vivo* tracking of hNSC-Mag$^+$ grafts in the mouse brain.** Study design of hNSC-Mag$^+$ transplantation via intracranial stereotaxic injection in mice, with contralateral internal controls of unlabeled hNSC (fimbria fornix target site indicated by "+") **(A)**. Representative serial T2* MRI sequence scans performed following transplantation on POD 7, 28, 42, 56, and 70; hNSC-Mag$^+$ grafts visible as hypointense signal or dark contrast at the targeted fimbria fornix site (red circle); unlabeled cell grafts were not visualized (green circle) **(B)**. Graft volume calculated from hypointense signal in T2* MR images for all time points **(C)**. Data are presented as representative MRI scans or mean ± SEM. Sample size of acquired MRI scans: POD 7 (n=9), POD 28 (n=6), POD 42-70 (n=3). Abbreviations: hNSC, human neural stem cells; MRI, magnetic resonance imaging; POD, postoperative day.

**Figure 5. Histological validation of MR signal in postmortem NHP brain.** Representative NHP POD 28 T2* MRI **(A)** with visible thalamus injection site (red box), and corresponding gross section **(B)** showing location of thalamus injection site assessed histologically (red circle), and location of medial

injection tracts en route to the thalamic and temporal site (arrows). Hematoxylin and eosin-staining shows infiltrating cells in injection area **(C)**. Negative STEM121 immunostaining in the same area with no intact hNSCs visible **(D)**. Immunostaining for CD3, CD68, and GFAP **(E-G)** indicating that infiltrating cells were primarily macrophages, with a smaller proportion of T lymphocytes, and a border of astrocytes. Perls' iron and immunostaining for MEs **(H-I)** within same area shows iron particles within macrophages and extracellularly. Scale bars 50 µm. Data are presented as representative images from a single NHP (n=1). Abbreviations: NHP, non-human primate; POD, postoperative day; MRI, magnetic resonance imaging; hNSC, human neural stem cells; CD3, cluster of differentiation 3; CD68, cluster of differentiation 68; GFAP, glial fibrillary acidic protein; ME, magneto-endosymbiont.

**Figure 6. Histological validation of MR signal in postmortem mouse brain.** Representative T2* MRI **(A,D,G)** and corresponding immunostaining of coronal whole brain showing on-target hNSC-Mag$^+$ graft in the fimbria fornix of the hippocampus **(B,E,H)** at terminal time points POD 7, 28, and 70. High power imaging **(C,F,I)** of highlighted hNSC-Mag$^+$ graft area (red box) and contralateral controls (green box) showing human-specific huNu (green) and ME particles (red). No ME staining was observed in control unlabeled hNSC graft areas (green boxes). Quantified MR signal volume **(J)**, huNu$^+$ nuclei indicating cell engraftment **(K)** and ME immunostaining **(L)** at terminal time points POD 7, 28, and 70. Correlations of MR signal and histological ME signal **(M)**, MR signal and cell engraftment **(N)**, and ME signal and cell engraftment **(O)**. *$p<0.05$, **$p<0.005$ (ANOVA). Scale bars 100 µm and 50 µm as indicated. Data are presented as representative images or mean ± SEM (n=3 per POD time point). Abbreviations: MRI, magnetic resonance imaging; POD, postoperative day; hNSC, human neural stem cells; huNu, human nuclei, ME magneto-endosymbiont.

**Figure 7. ME labeling does not impact *in vivo* phenotype of transplanted hNSC grafts.**

Representative immunostaining of hNSC and hNSC-Mag$^+$ grafts for NeuN, GFAP, and hNestin differentiation markers (red) with huNu (green) at terminal time points POD 7, 28, and 70. Images show regions of interest containing huNu$^+$ grafts or injection tracts within the targeted fimbria fornix area, as indicated by dashed lines. Scale bar 100 µm. Data are presented as representative images (n=3 per POD time point). Abbreviations: hNSC, human neural stem cells; POD, postoperative day; NeuN, neuronal nuclei; GFAP, glial fibrillary acidic protein; hNestin, human nestin; huNu, human nuclei.

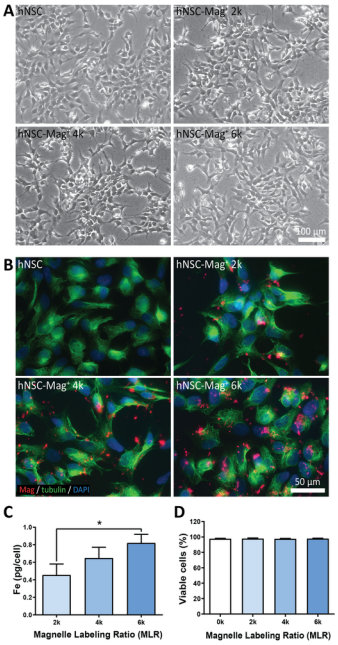


SCT3_12802_Figure_1.tif

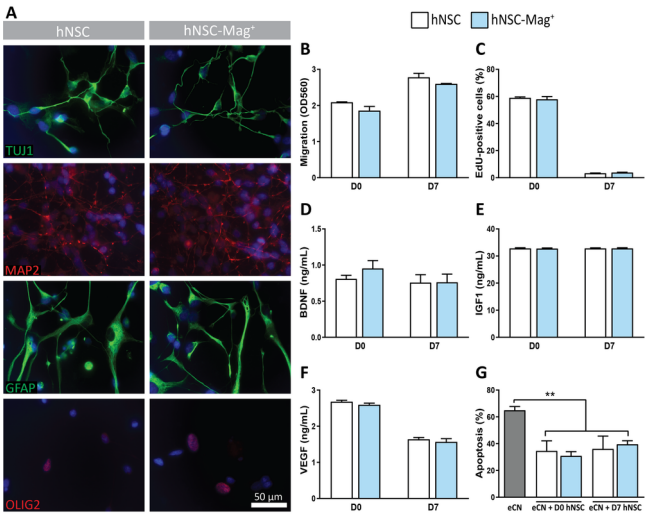


SCT3_12802_Figure_2.tif

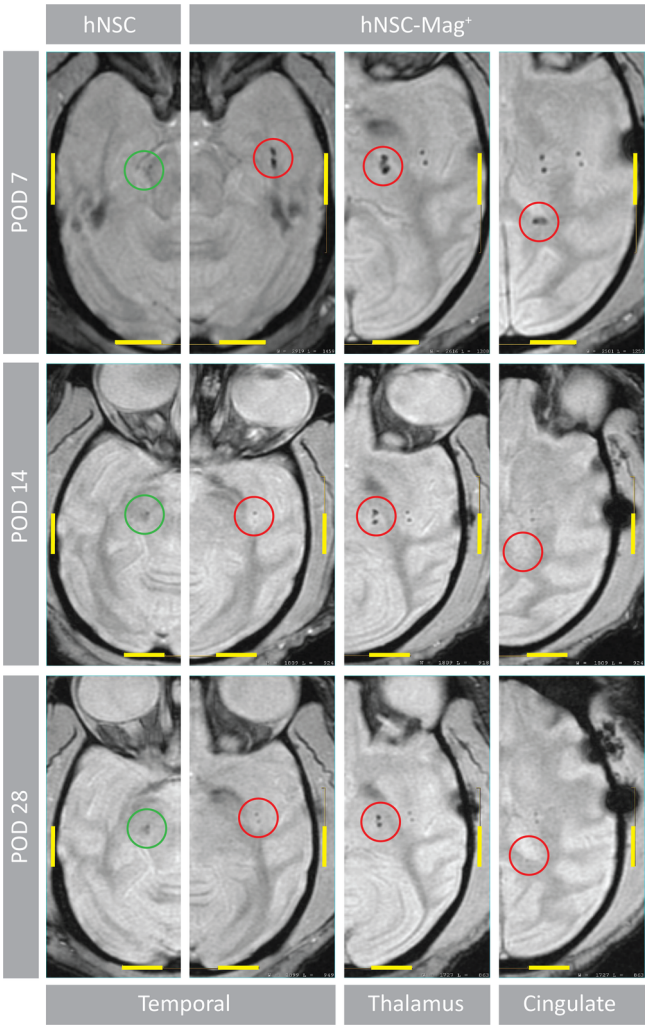


SCT3_12802_Figure_3.tif

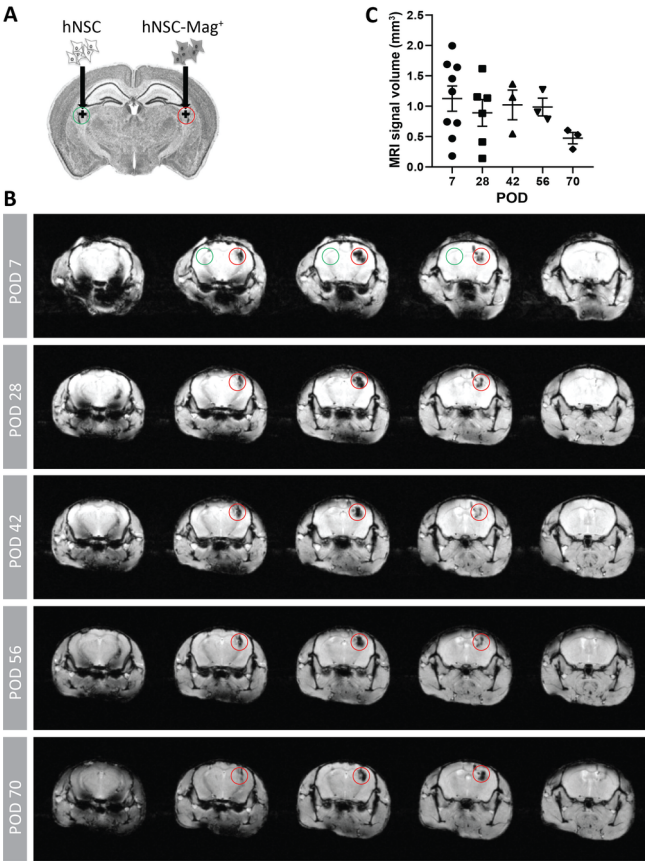


SCT3_12802_Figure_4.tif

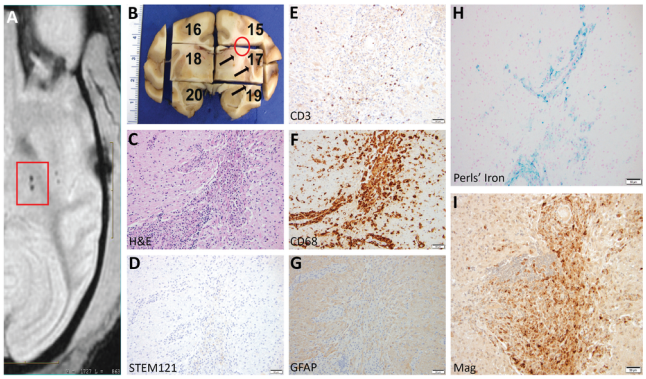


SCT3_12802_Figure_5.tif

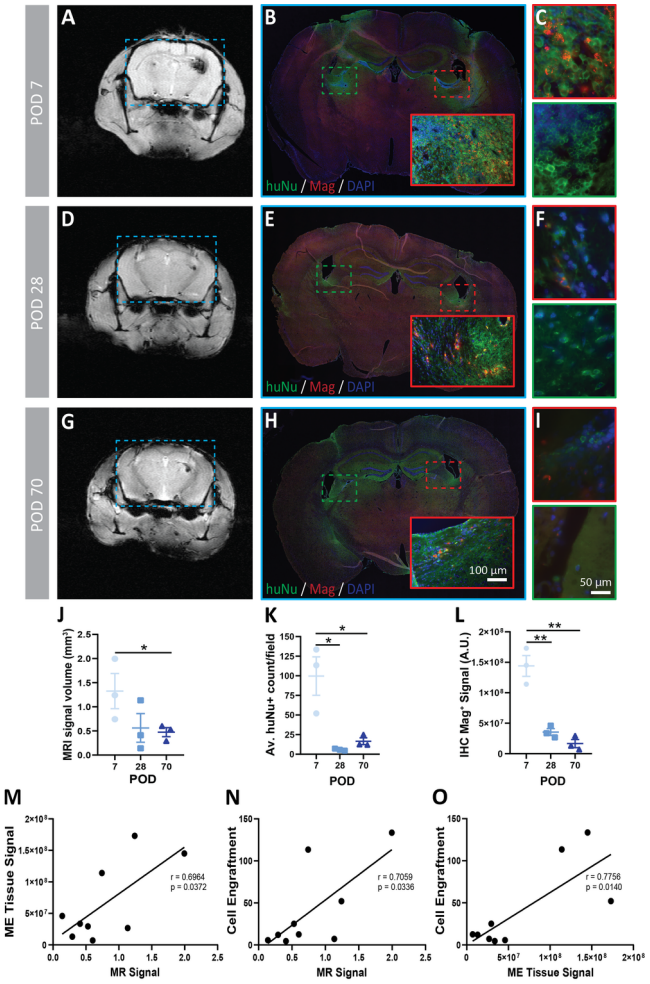


SCT3_12802_Figure_6.tif

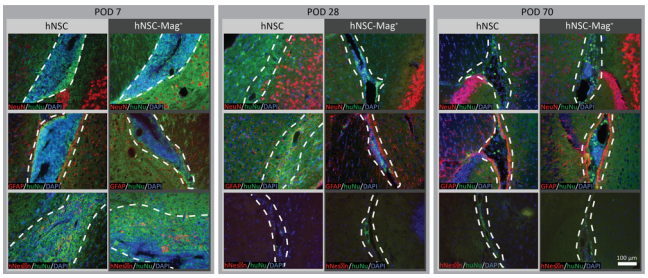


SCT3_12802_Figure_7.tif

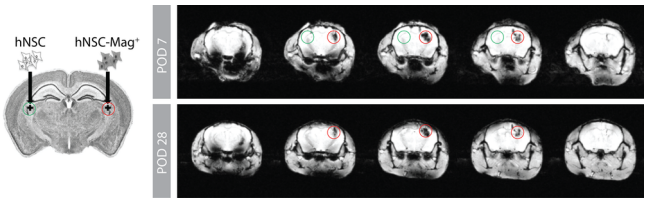


SCT3_12802_Graphical Abstract.tif